BN/Cs_2CO_3/TiO_2 composite nanofibers to improve hydrogen generation

Massomeh Ghorbanloo, Amr Nada, Heba El-Maghrabi, Maged Bekheet, Wiebke Riedel, Roman Viter, Stéphanie Roualdes, Philippe Miele, Mikhael Bechelany

BN/Cs_2CO_3/TiO_2 composite nanofibers to improve hydrogen generation

Massomeh Ghorbanloo[a,b,*] , Amr Nada[a,c,*], Heba El-Maghrabi[a,d], Maged Bekheet[e], Wiebke Riedel[f], Roman Viter[g,h], Stéphanie Roualdes[a], Philippe Miele[a], Mikhael Bechelany[a,*]

[a] Institut Européen des Membranes, IEM, UMR 5635, Univ Montpellier, ENSCM, CNRS, Montpellier, France

[b] Chemistry Department, Faculty of Science, University of Zanjan, Zanjan, Iran.

[c] Department of Analysis and Evaluation, Egyptian Petroleum Research Institute, Cairo 11727, Egypt

[d] Department of Refining, Egyptian Petroleum Research Institute, Cairo 11727, Egypt.

[e] Technische Universität Berlin, Faculty III Process Sciences, Institute of Material Science and Technology, Chair of Advanced Ceramic Materials, Straße des 17. Juni 135, 10623 Berlin, Germany

[f] Institut für Chemie, Freie Universität Berlin, Arnimallee 22, 14195 Berlin, Germany

[g] Institute of Atomic Physics and Spectroscopy, University of Latvia, 19 Raina Blvd., LV 1586 Riga, Latvia

[h] Sumy State University, Center for Collective Use of Scientific Equipment 31, Sanatornaya st., 40018 Sumy, Ukraine

* Corresponding author: m_ghorbanloo@yahoo.com, chem_amr@yahoo.com & mikhael.bechelany@umontpellier.fr

Abstract

This study describes the synthesis of cesium carbonate-titanium dioxide (Cs_2CO_3/TiO_2) and boron nitride-cesium carbonate-titanium dioxide (BN/Cs_2CO_3/TiO_2) nanofiber photocatalysts by electrospinning. The nanofiber properties were modulated by varying Cs_2CO_3 mole percentage. In all prepared nanofibers, the anatase TiO_2 structure was the main phase. Cs_2CO_3 addition in the electrospinning mixture led to the formation of small amounts of rutile phase and decreased the anatase phase crystallinity. The highest photocatalytic activity was observed with the Cs_2CO_3/TiO_2 photocatalyst that included 1.5 mol% of Cs_2CO_3. Indeed, hydrogen production rate (9,853 $\mu mol \cdot g^{-1} \cdot h^{-1}$) was 89.6 times higher than with pure TiO_2

nanofibers. Modification of the 1.5% Cs_2CO_3/TiO_2 photocatalyst with hexagonal BN further increased hydrogen production up to 15,823 μmol/g (6 h under visible light). This improvement could be explained by the presence of BN sheets in the $BN/Cs_2CO_3/TiO_2$ catalyst that improve the separation of the photoinduced electron–hole pairs in TiO_2 and increase the specific surface area compared with pure TiO_2 and Cs_2CO_3/TiO_2 nanofibers.

Keywords: *Cesium carbonate nanofibers; Electrospinning; Photocatalysis; Hydrogen evolution; Boron nitride; Water splitting.*

1. Introduction

Hydrogen (H_2) is an environmentally acceptable, alternative energy carrier that can be easily stored and displays high conversion efficiency and recyclability. Therefore, it could play a major role in addressing energy demands and environmental pollution [1-6]. Several H_2 production methods based on clean-energy technologies have been investigated, including photocatalytic [7-9], electrocatalytic [10-12] and photoelectrocatalytic [13, 14] water splitting. Photocatalytic water splitting is particularly interesting because solar energy is cheap, abundant and green [15].

As the visible light represents ~46% of the solar spectrum, developing a visible light-responsive photocatalyst with a narrow band gap is a major challenge. Heterogeneous semiconductor photocatalysts are excellent candidates for photocatalytic H_2 evolution using visible light mainly due to their stability, wide absorption region of visible light, lower recombination rate, and robust redox capacity [16-18].

Fujishima and Hondain [19] were the first to describe titanium dioxide (TiO_2)-based semiconductors for H_2 production. Then, various TiO_2 modification strategies were investigated to obtain heterogeneous semiconductors (e.g. doping and co-doping with metal and/or non-metal elements [20-26], surface fluorination [27], surface sensitization to visible light with graphene and with hexagonal boron nitride, *h*-BN [28-30]). Metal doping improves the photocatalytic activity of TiO_2-based semiconductors by promoting the electron-hole (e^-/h^+) pair separation and by increasing the charge separation efficiency and the number of catalytically active sites on the TiO_2 surface [31, 32]. Moreover, *h*-BN can increase the reactant capacity to absorb light, limit e^-/h^+ recombination in TiO_2 [33], [34], and enhance TiO_2 photocatalytic activity.

TiO_2 photocatalytic efficiency and electron transport are influenced by the photocatalyst shape and morphology (e.g. nanoparticles, nanotubes, nanoflowers, nanofibers) [35-38]. One-dimensional (1D) nanofibers display high specific surface area and porosity, form fewer aggregates, and promote charge transfer [39] and electron transport. These features explain their high photocatalytic efficiency for H_2 generation [2, 40, 41]. Different techniques can be used for TiO_2 nanofiber synthesis [42-46]. Among them, electrospinning is a cheap, simple and excellent method to fabricate 1D TiO_2 nanofibers with very long pure phase length, higher crystallinity, larger surface area to volume ratio, and controlled morphology and chemical composition [34].

TiO_2 photocatalytic activity can also be improved by metal ions [47]. Here, we used Cs^{+1} because of their high electron trapping efficiency that enhances the charge separation efficiency and e^-/h^+ accumulation at energy bands with high redox potential [48]. Hezam *et al*. suggested that coupling TiO_2 with Cs^{+1} could reduce TiO_2 band gap and e^-/h^+ recombination rate, thus improving its photocatalytic activity. They showed that Cs^{+1} lead to a red shift toward a longer wavelength in the TiO_2 nanoparticle absorption spectrum and increase the interfacial electron transfer rates, thus reducing the e^-/h^+ pair recombination rate [48].

Here, we investigated the synergetic effect of *h*-BN and Cs cation addition on the photocatalytic efficiency of TiO_2 composite nanofibers during H_2 generation. The main goal of this work was to use electrospinning to fabricate cesium carbonate-TiO_2 (Cs_2CO_3/TiO_2) and boron nitride-Cs_2CO_3/TiO_2 (BN/Cs_2CO_3/TiO_2) nanofibers to be used as photocatalysts in the presence of visible light [49] for green H_2 production.

2. Experimental section

2.1. Materials

Cs_2CO_3 (99.95%, Mw = 325.82 g/mol), titanium tetraisopropoxide (TTIP) ($Ti(OCH(CH_3)_2)_4$, 97%), polyvinylpyrrolidone (PVP; M_w=1300000 g/mol), acetic acid (98%), absolute ethanol (99%), absolute methanol (99%), N,N-dimethylformamide (DMF; 99.8%), Nafion perfluorinated resin solution, and gelatin from porcine skin were from Sigma Aldrich. All chemicals were used as received.

2.2. Preparation of Cs_2CO_3/TiO_2 composite nanofibers

Cs_2CO_3/TiO_2 nanofibers with different mole percentages (mol%) of Cs_2CO_3 relative to TiO_2 (0.25, 0.5, 1, 1.5, and 2.5 mol%) were fabricated by electrospinning. Briefly, 0.3 g of PVP was added to the TTIP suspension in ethanol (3 mL) and acetic acid (2 mL) under stirring at room temperature for 30 min (precursor solution). Then, Cs_2CO_3 (different mol%) was dissolved in ethanol (2 mL) and DMF (0.5 mL) by stirring for 30 min, and added to the precursor solution. The mixture was vigorously stirred for 1 h and when homogeneous, it was transferred to a syringe with a stainless-steel needle (0.7 mm in diameter). Electrospinning was performed with a constant flow rate of 1 mL/h, chamber temperature of 38 ± 5 °C, and high voltage power (1.25 kV/cm). Nanofibers were collected on a rotating coil (rotation speed of 400 rpm) covered with aluminum, followed by calcination in a furnace at 400 °C (heating rate of 5 °C/min) in air for 4 h.

2.3. BN exfoliation

For BN exfoliation [50], 20 g of porcine skin gelatin was added to 80 mL of hot water (70 °C) followed by 1 g of BN powder. The mixture was kept in an ultrasonic homogenizer at 50 °C overnight. Exfoliated BN was collected by centrifugation at 6000 rpm for 30 min followed by supernatant decantation. The precipitate (exfoliated BN) was dried at 80 °C for 48 h and then calcined at 600 °C (heating rate of 5 °C/min) for 2 h in air to obtain pure exfoliated BN.

2.4. Preparation of BN/TiO_2 and BN/1.5% Cs_2CO_3/TiO_2 composite nanofibers

BN/TiO_2 and BN/1.5% Cs_2CO_3/TiO_2 composite nanofibers were fabricated by electrospinning as previously reported [34]. Briefly, the mixture containing PVP, TTIP and Cs_2CO_3 was prepared as described in section 2.2. Then, 5 mg of pure exfoliated BN in ethanol was added after sonication and the mixture was stirred at room temperature for 1 h. Electrospinning, nanofiber collection, and calcination were performed as described in section 2.2.

2.5. Sample characterization

The nanofiber crystal structure was evaluated using a PANAlytical Xpert-PRO diffractometer, equipped with an X'celerator detector, and Ni-filtered Cu-radiation (CuKα1 radiation wavelength: 0.1540598 nm, and CuKα2 radiation wavelength: 0.1544426 nm) at 40 kV and 40 mA. To obtain good quality X-ray diffraction (XRD) patterns, nanofibers were finely

ground to powder and then scanned within 2h at a scanning rate of 0.1° min^{-1} (step size and time: 0.02° and 12s) and range of 10–90°. Their morphology and structure were studied by scanning (SEM; Hitachi S4800, Japan) and transmission electron microscopy (TEM; JEOL JEM 2100, JEOL, Japan) at an accelerating voltage of 200 kV. Their composition was analyzed by energy-dispersive X-ray spectroscopy (EDX) and elemental mapping using a Zeiss EVO HD15 microscope coupled with an Oxford X-MaxN EDX detector. Raman spectra were generated by dispersive Raman spectroscopy (Model Sentera, Bruker, Germany) at 532 nm with a neodymium-doped yttrium aluminum garnet (power of 60 mW). Fourier transform infrared (FTIR) spectra were recorded using KBr disks and a Nicolet 370 FTIR spectrometer. The nanofiber band gap was measured with a UV–Vis spectrophotometer (Jasco model V-570) equipped with a diffuse reflectance attachment (Shimadzu IRS-2200). Photoluminescence spectra were recorded using an optical fiber spectrometer (Ocean Optics usb2000). Continuous wave (cw) Electron Paramagnetic Resonance (EPR) measurements at X-band frequencies (9.862 GHz) were done at room temperature in quartz tubes of 2.9 mm outer diameter, with a Bruker B-ER420 spectrometer upgraded with a Bruker ECS 041XG microwave bridge and a lock-in amplifier (Bruker ER023M); a modulation amplitude of 2 G and a modulation frequency of 100 kHz were applied with a Bruker SHQ resonator. All EPR spectra were normalized to the sample mass. Elemental analysis was done by inductively coupled plasma optical emission spectroscopy with a Horiba Scientific ICP Ultima2 (Horiba, Japan). The elemental composition was investigated by X-ray photoelectron spectroscopy (XPS) on an Escalab 250 (Thermo Fisher Scientific, USA) using monochromatic Al K α (1486.6 eV) at 2 kV and 1 μA (analysis of 400 μm of surface diameter with an acquisition time of 1203.5 s).

2.6. Photochemical measurements

Electron/hole generation, migration, and recombination were monitored by photocurrent response and electrochemical impedance spectroscopy (EIS) with a ModuLap XM potentiostat (Solartron Analytical, USA), a three-electrode cell, 0.5M Na_2SO_4 aqueous solution as electrolyte, Pt wire as counter electrode, Ag/AgCl as reference electrode, and $BN/Cs_2CO_3/TiO_2$ coated on indium–tin–oxide (ITO) as working electrode. The light source was a 500 W linear halogen lamp (λ range = 420 to 600 nm and frequency range = 10^{-2} to 105 Hz). The working electrode was prepared by depositing 40 μL of nanocomposite suspension

onto the ITO surface (10 × 10 mm) followed by drying at room temperature. The suspension was prepared by ultrasonic dispersion of 5 mg of photocatalyst in 80 μL deionized water, 20 μL ethanol, and 40 μL Nafion followed by ultrasonication for 60 min. The EIS data were analyzed and fitted to the equivalent circuit with the EC-Lab software. The photocurrent *vs.* irradiation time curve was recorded at 0.0 V/SCE to 1.1 V/SCE in the dark (20 s) and in the presence of light (20 s) at a scan rate of 10 $mV \cdot s^{-1}$.

2.7. Photocatalytic H_2 generation

H_2 was produced by photocatalysis in an air-tight quartz reactor, in which the reaction temperature was maintained at 25 °C by a cold-water circulation system. The irradiation source was a 500 W linear halogen lamp that emitted light with a spectrum between 420 and 600 nm [51]. The lamp-aqueous solution distance was 10 cm. Briefly, nanofibers (50 mg) were dispersed in 20 mL of 20% methanol aqueous solution (i.e. the scavenger) and transferred to the reactor. Oxygen was removed from the reaction medium by pre-purging with nitrogen for 30 min. Gas samples were collected each hour to assess H_2 production by gas chromatography (GC-1690, Jiedao, TCD, Ar carrier) with a 5 Å molecular sieve column (3 m × 2 mm).

3. Result and Discussion

In this study, TiO_2 was modified with Cs_2CO_3 and also with *h*-BN nanosheets to increase its photocatalyst activity in water splitting reactions. The effects of TiO_2 structure and morphology, of Cs_2CO_3 and *h*-BN addition, and of methanol as sacrificial reagent on the photocatalytic activity of TiO_2 were investigated.

3.1. Structural and morphological properties of the different composite nanofibers

XPS analysis of Cs_2CO_3-TiO_2 physicochemical interactions showed that the two peaks detected at 458.55 eV and 464.26 eV in the Ti 2p XPS spectra corresponded to $2p_{3/2}$ and $2p_{1/2}$ (Fig. 1a) [52]. Upon Cs_2CO_3 addition, the Ti peaks were shifted to lower binding energies: decrease by 0.12 eV for BN/TiO_2, 0.55 eV for 1.5% Cs_2CO_3/TiO_2, and 0.67 eV BN/1.5% Cs_2CO_3/TiO_2 nanofibers. This shift can be explained by the decreased Ti oxidation state in the presence of BN or Cs_2CO_3 and the higher Ti reduction in the BN/1.5% Cs_2CO_3/TiO_2 sample due to the BN and Cs_2CO_3 synergism [53]. It also suggests that Cs_2CO_3 is connected with the TiO_2 surface [54, 55].

The O 1s XPS spectra (Fig. 1b) also contained two peaks: one at ~529.7 eV identical to the oxygen in lattice (O_{latt}) and another at ~ 532 eV that corresponded to surface oxygen [53]. O 1s peaks were shifted to lower binding (~0.5 eV) upon addition of 1.5 mol% Cs_2CO_3 compared with TiO_2 and BN/TiO_2 nanofibers [54, 55]. Similarly, Cs_2CO_3 addition decreased the binding energy of B 1s and N 1s by ~0.3 eV (Fig. 1c-d). This demonstrated Cs_2CO_3 connection with the BN and TiO_2 nanofiber surface.

Cs_2CO_3 presence in TiO_2 nanofibers was confirmed by the peaks at 723.8 and 737.7 eV (i.e. $3d_{5/2}$ and $3d_{3/2}$ of Cs_2CO_3) [54, 55] in the Cs 3d spectra (Fig. 1e).

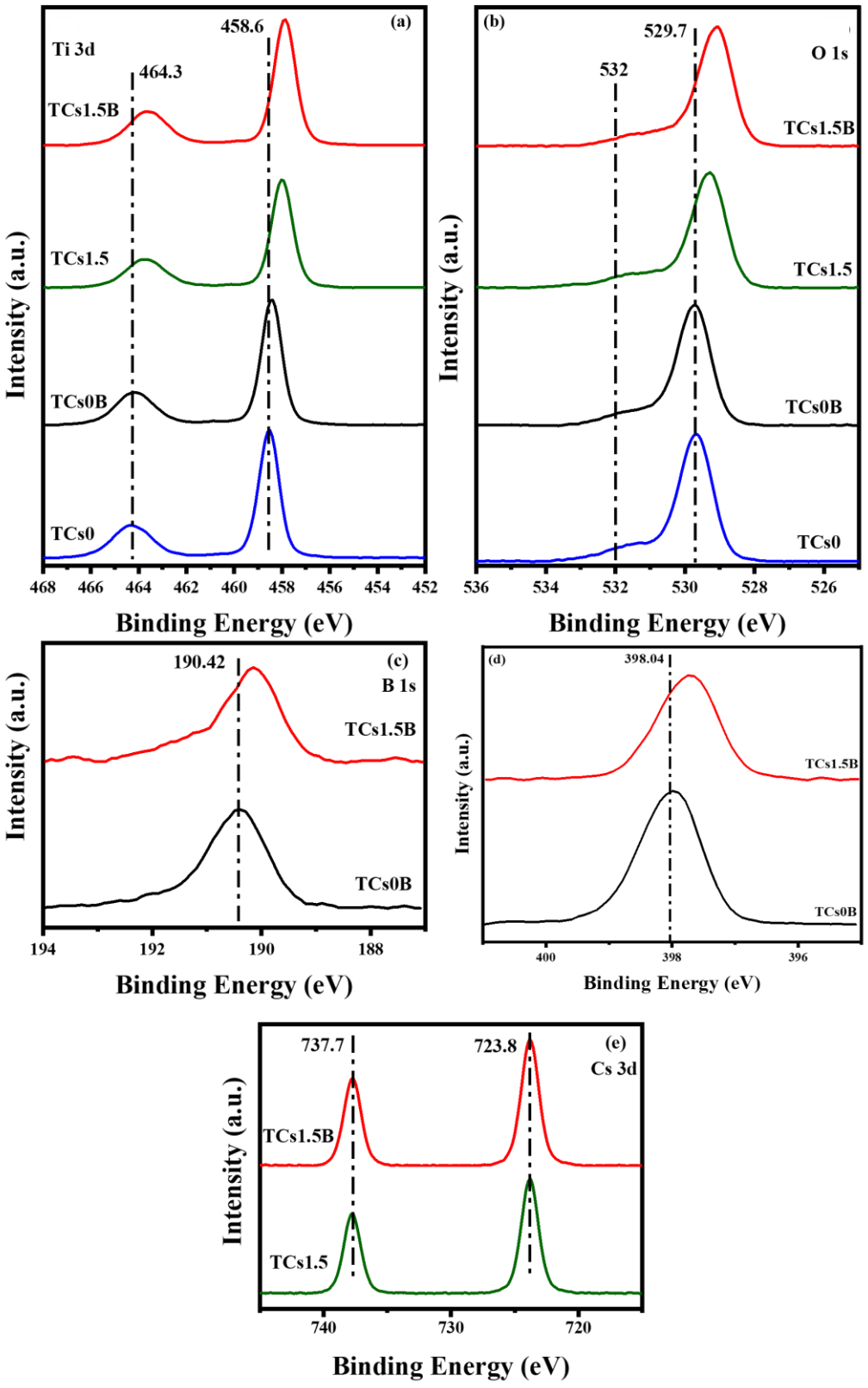

Fig. 1. High-resolution XPS spectra of Ti 2p (a), O 1s (b), B 1s (c), N 1s (d) and Cs 3d (e) for TiO_2 nanofibers without (TCs0), and with 1.5 mol% Cs_2CO_3 (TCs1.5) and for BN/TiO_2 (TCs0B) and BN/1.5% Cs_2CO_3/TiO_2 (TCs1.5B) nanofibers.

Analysis of crystallinity and phase composition showed in all nanofiber samples the typical XRD reflections of anatase TiO_2 (JCPDS No. 01-084-1285) at $2\theta = 25.3^0$, 37.8^0, 47.9^0, 53.9^0, 55.1^0 and 62.6^0 (Fig. 2a) that were attributed to the (101), (004), (200), (105), (211) and (204) diffraction planes of anatase TiO_2 [56]. The anatase phase crystallinity was reduced upon Cs_2CO_3 addition (at different mol%) as well as the crystallite size of the anatase phase, calculated from the peak broadening using the Scherrer equation (from 16±1 nm in the sample without Cs_2CO_3 to ~6±1 nm in the composite samples with different Cs_2CO_3 amounts). Minor amounts of rutile and brookite phases were observed in the Cs-containing nanofibers. Conversely, neither XRD reflections corresponding to any crystalline Cs-containing compound nor remarkable shifts in Cs-containing nanofibers were observed in the composite samples compared with the pure TiO_2 sample. This suggests that Cs^{1+} ions do not take the place of Ti^{4+} ions in the lattice of the anatase or rutile phase, likely due to the large ionic radius difference between Ti^{4+} and Cs^{1+} (60.5 pm vs 167 pm; all cations are 6-fold coordinated) [57]. Indeed, the substitution of smaller Ti^{4+} by larger Cs^{1+} cations should be accompanied by an increase in the TiO_2 lattice parameter and unit cell volume. These results are in good agreement with our previous studies [58] showing that large ions (e.g. Ce^{3+}) cannot enter the TiO_2 lattice, but may take the place of Ti^{4+} ions on the TiO_2 crystallite surface. This leads to their binding to Ti-O networks on the TiO_2 crystallite surface that limits the anatase phase growth by reducing the interactions between crystallites and the Ti and O atom rearrangement in the lattice. As a result, the crystallite size of Cs-containing TiO_2 nanofibers was reduced. Lastly, the XRD reflections at $2\theta = 26.6^0$ and 41.9°, corresponding to the (002) and (100) diffraction planes of *h*-BN, confirmed *h*-BN incorporation in the BN/TiO_2 and BN/1.5% Cs_2CO_3/TiO_2 samples [59]. BN addition led to a decrease in the crystallite size of the anatase phase to 6±1 nm and the formation of small amounts of brookite phases.

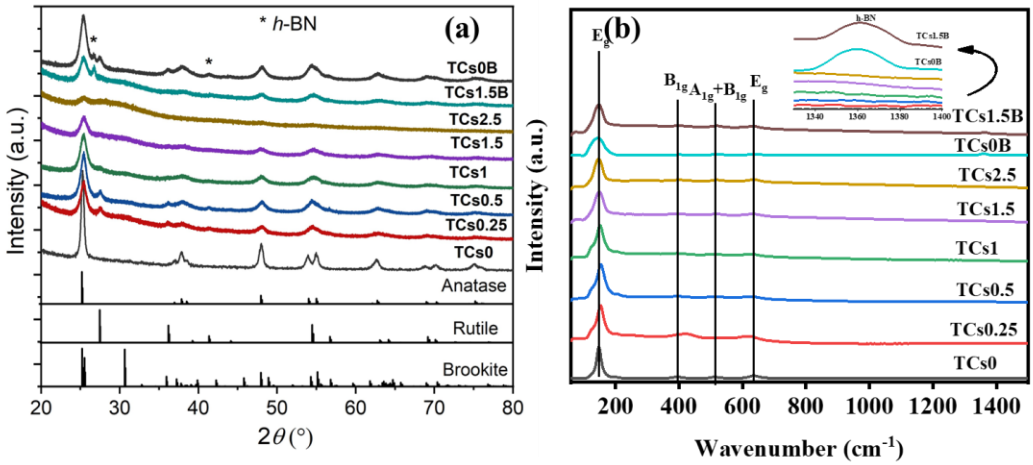

Fig. 2 (a) XRD patterns and (b) Raman spectra of TiO_2 (TCs0) nanofibers, and of 0.25% Cs_2CO_3/TiO_2 (TCs0.25), 0.5% Cs_2CO_3/TiO_2 (TCs0.5), 1% Cs_2CO_3/TiO_2 (TCs1), 1.5% Cs_2CO_3/TiO_2 (TCs1.5), 2.5% Cs_2CO_3/TiO_2 (TCs2.5), BN/TiO_2 (TCs0B) and BN/1.5% Cs_2CO_3/TiO_2 (TCs1.5B) composite nanofibers.
Inset: excitation spectra monitored at 1360 cm^{-1}.

.

The Raman spectra of all samples (Fig. 2b) included the Raman-active modes of TiO_2 anatase phase at 147.9 cm^{-1} (E_g), 197.2 cm^{-1} (E_g), 396.8 cm^{-1} (B_{1g}), 513.3 cm^{-1} ($A_{1g}+B_{1g}$), and 635.7 cm^{-1} (E_g) [60]. The Raman spectra of the BN/TiO_2 and BN/1.5% Cs_2CO_3/TiO_2 samples displayed a peak at 1362 cm^{-1} attributed to the E_2g mode of *h*-BN [50]. Compared with the TiO_2 sample, after Cs_2CO_3 addition the vibration peaks were characterized by a slight blue shift and wider width. These changes are explained by the destroyed anatase lattice and formation of small rutile and brookite amounts and by Cs_2CO_3 effects on the nanofiber surface [34, 61]. Moreover, strong chemical interactions between TiO_2 and *h*-BN nanofibers could influence the TiO_2 lattice vibrational characteristics, leading to asymmetric peak broadening, besides the Cs_2CO_3 effect highlighted by XPS [62].

In addition, in the FTIR spectra of TiO_2 without and with Cs_2CO_3 and/or *h*-BN, the peak at 650-900 cm^{-1} and the weak bands at 2800-2900 cm^{-1} were due to Ti–O bonding [50] and C-H bonds from organic precursors, respectively (Fig. S1). In the FTIR spectra of BN-containing samples, the bands at 800 and 1381 cm^{-1} were caused by out-of-plane bending of sp^2-bonded B–N–B and in-plane stretching of sp^2-bonded B–N, respectively [63]. The new bands at 1370 cm^{-1} were caused by B-O-Ti vibrations [64]. The additional peaks at 1238 cm^{-1} and 894 cm^{-1}, attributed to B–O in-plane and out-of-plane bending, demonstrated B-O

bonding in *h*-BN nanosheets [65]. Moreover, the typical bands in the fingerprint areas were slightly shifted, showing strong interactions between *h*-BN and TiO_2 [66]. This suggests the synthesis of *h*-BN-TiO_2 composites.

EDX analysis of several nanofibers in each sample confirmed Cs^{1+} incorporation in TiO_2 nanofibers. The Cs^{1+}/Ti^{4+} atomic ratio increased with Cs_2CO_3 amount (2.5 > 1.5 > 1 > 0.5 > 0.25 mol%), in agreement with the experimental values. The elemental mapping image (Fig. S3) showed that Cs and BN were homogeneously and evenly distributed on TiO_2 surface in the BN/1.5% Cs_2CO_3/TiO_2 sample.

Additionally, atomic absorption spectroscopy showed that the Ti:Cs atomic ratio in 1.5% Cs_2CO_3/TiO_2 and BN/1.5% Cs_2CO_3/TiO_2 composite nanofibers was approximately 1.598:0.024. The Ti:Cs mole ratio in the electrospinning mixture was 0.985:0.015. This suggests that the Cs precursor was effectively loaded on TiO_2 nanofibers because the Cs quantity in the produced samples was similar to the concentration used in the electrospinning tests. Furthermore, the identical Ti and Cs contents in 1.5% Cs_2CO_3/TiO_2 and BN/1.5% Cs_2CO_3/TiO_2 composite nanofibers suggest that nanofiber composites are reproducible.

The morphology and structure of the photocatalysts were assessed by SEM and TEM. SEM images of the as-synthesized composite nanofibers (Fig. 3a-h) showed that all samples were composed of a highly interconnected network of continuous, randomly oriented TiO_2 nanofibers. Moreover, the nanofiber diameter decreased from 240 nm in pristine TiO_2 to 115 nm, 70 nm, and 57 nm in 3% Cs_2CO_3/TiO_2, BN/TiO_2, and BN/3% Cs_2CO_3/TiO_2 nanofibers, respectively (Fig. S2). The nanofiber diameter reduction with increasing Cs concentrations could be attributed to the difference between Ti^{4+} and Cs^{1+} ionic radius that may cause a perturbation in the anatase crystal structure, thus hindering crystal growth [67]. To confirm Cs_2CO_3 homogeneous distribution with TiO_2, nanofibers were analyzed by high-resolution TEM (Fig. 3i and j). The tetragonal structure of TiO_2 in pristine TiO_2 nanofibers and in BN/1.5% Cs_2CO_3/TiO_2 composite nanofibers was confirmed by their interplanar spacing (0.35 nm and 0.31 nm, respectively) that corresponded to the (101) plane (Fig. 3i and j, inset). The d spacing decrease in BN/1.5% Cs_2CO_3/TiO_2 compared with TiO_2 nanofibers indicates d-spacing shrinking due to the effect of BN and Cs_2CO_3 on TiO_2 lattice. The selected area electron diffraction (SAED) patterns of TiO_2 and BN/1.5% Cs_2CO_3/TiO_2 samples are in the inset of Figure 3i and j. Upon Cs_2CO_3 incorporation, crystallinity changed from pure anatase to a polycrystalline structure.

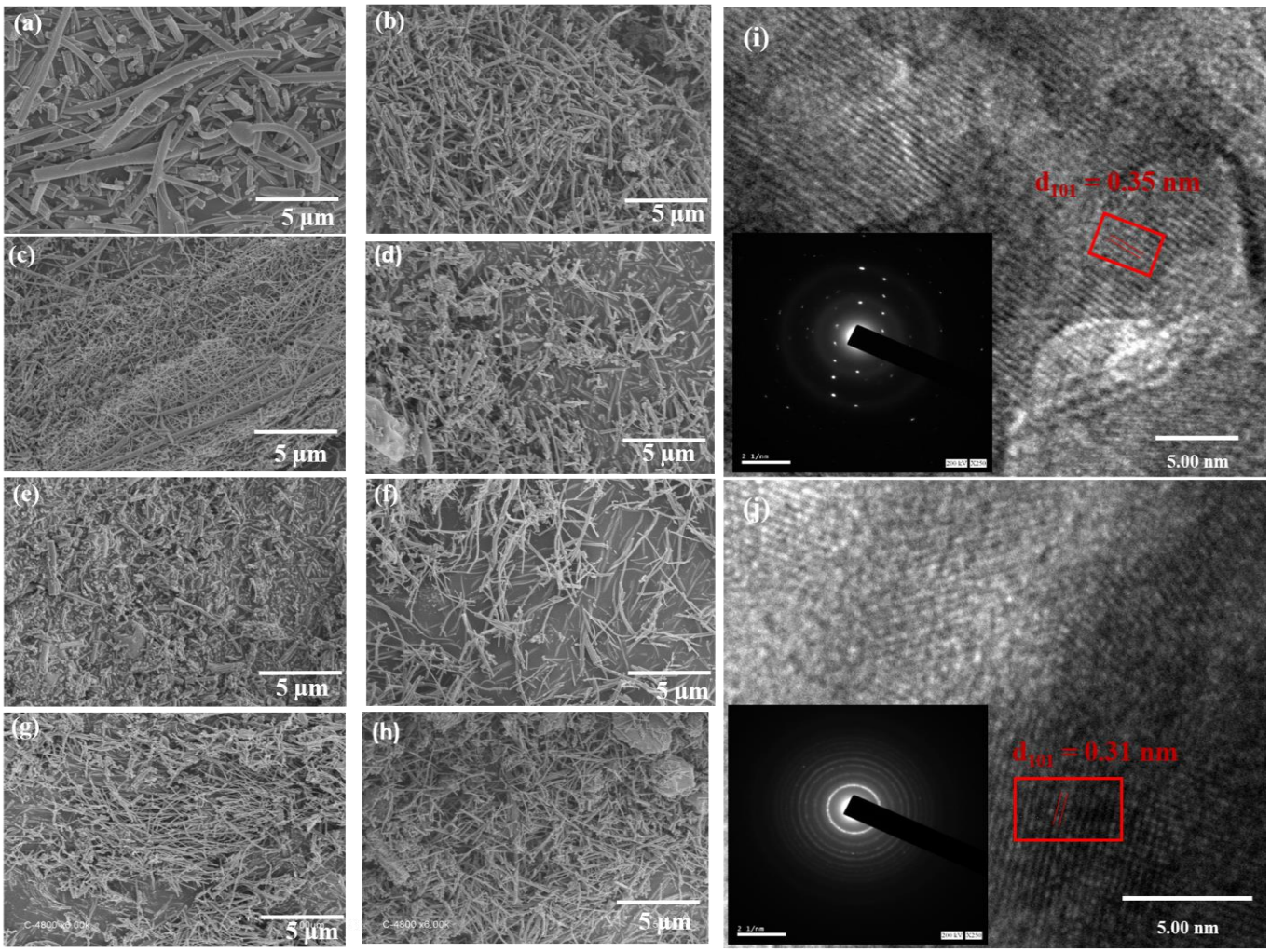

Fig. 3 SEM images of a) pristine TiO_2, b) 0.25% Cs_2CO_3/TiO_2, c) 0.5% Cs_2CO_3/TiO_2, d) 1% Cs_2CO_3/TiO_2, e) 1.5% Cs_2CO_3/TiO_2, f) 2.5% Cs_2CO_3/TiO_2, g) BN/TiO_2, h) BN/1.5% Cs_2CO_3/TiO_2 after calcination at 400 °C, and high-resolution TEM images of i) pristine TiO_2 and j) BN/1.5% Cs_2CO_3/TiO_2 with the respective selected area diffraction patterns in the inset.

Brunauer-Emmett-Teller (BET) surface area measurements further demonstrated that Cs_2CO_3 presence resulted in a reduction in the size of the crystallites and diameter of the generated nanofibers. The surface area should increase as the crystallite size shrinks. According to the BET results, the surface areas of TiO_2, 0.25% Cs_2CO_3/TiO_2, 0.5% Cs_2CO_3/TiO_2, 1.0% Cs_2CO_3/TiO_2, 1.5% Cs_2CO_3/TiO_2, 2.5% Cs_2CO_3/TiO_2, BN/TiO_2, and BN/1.5% Cs_2CO_3/TiO_2 were 11, 29, 39, 50, 62, 68, 15, and 70 $m^2\ g^{-1}$, respectively. It is worth noting that the surface area increase is a key factor for improving the catalytic activity [68, 69]. The larger specific surface area of BN/1.5% Cs_2CO_3/TiO_2 could allow the rapid diffusion of reactants and products, thus enhancing the photocatalytic reaction [34, 70].

As the nanofiber photocatalytic activity is linked to the formation of oxygen vacancies, the EPR spectra of the different composites were generated. In the room temperature cw EPR measurements at 9.86 GHz (Fig. 4a), a relatively sharp, symmetrical line ($\Delta B_{pp} \approx 5$ G) of g = 2.003-2.004 was detected. A similar symmetrical EPR signal was previously described for TiO_2 samples and was attributed to electron trapping at an oxygen vacancy [71-74]. Compared with pristine TiO_2, this signal slightly increased upon addition of low Cs_2CO_3 concentrations (≤1 mol%; g close to 2.004 and $\Delta B_{pp} \approx 6$ G), and clearly decreased after incorporation of higher Cs_2CO_3 amounts, particularly 1.5 mol% Cs_2CO_3. Similarly, after BN incorporation, the signal intensity decreased and g values were slightly shifted, compared with pure TiO_2. In the BN/1.5% Cs_2CO_3/TiO_2 composite sample, EPR signal intensity was slightly lower than in the BN/TiO_2 sample, but higher than in the 1.5% Cs_2CO_3/TiO_2 composite. These observations indicate that addition of both BN and Cs does not strongly affect the EPR active defects, presumably located mainly at the surface, compared with the single addition of Cs or BN. On the other hand, both Cs and BN significantly reduced the number of the EPR active defects. It should be noted that EPR active defects are only a subset of all defects that are found in TiO_2 and that may also be affected by BN or Cs.

Then, the optical band gap of the prepared TiO_2 nanofibers was investigated by UV–vis absorbance measurements (Fig. 4b) and their band gap energy (Eg) was estimated with the Kubelka– Munk formula [56]:

$$F = ((1-R)^2)/2R \quad (1)$$

$$(Fhv)^{1/2} = A(hv-Eg) \quad (2)$$

where F, R, hν, and Eg are the Kubelka–Munk function, reflectance, photon energy and band gap, respectively.

Comparison of the Eg values of the different samples (Table 1) showed that upon Cs_2CO_3 incorporation in TiO_2 nanofibers, Eg increased from 3.18 eV (pristine TiO_2) to 3.36 eV (2.5% Cs_2CO_3/TiO_2). The blue-shifted band gap (related to Eg increase) might be due to the reduction of TiO_2 grain size following Cs_2CO_3 incorporation, as confirmed by the XRD data.

As XPS measurements indicated that Cs^+ cannot replace Ti^{4+}, no bulk Cs doping of TiO_2 was expected. However, in TiO_2-Cs_2CO_3 heterostructures, TiO_2 work function is

reduced and Fermi level position is increased [75-77]. The formed Cs_2CO_3 nanolayer surface results in an increase of free electron concentration on the surface area. The results correlate with data obtained in [78], where Cs_2CO_3 addition to TiO_2 resulted in an increase of the charge concentration to 10^{27}-10^{28} m^{-3}.

In the photoluminescence spectra of Cs_2CO_3/TiO_2 nanofibers (Fig. 4c), the observed peaks in the wavelength range of visible light corresponded to oxygen vacancies [79]. Introduction of Cs_2CO_3 and BN in TiO_2 structure led to photoluminescence quenching. It was reported that the free electron lifetime in Cs_2CO_3/TiO_2 nanostructures is shorter than in unmodified TiO_2 [75]. This explains the photoluminescence intensity decrease of Cs_2CO_3/TiO_2 nanostructures. The photoluminescence intensity reduction of BN/TiO_2 nanostructures could be due to a charge separation increase [80].

In agreement with the EPR results, photoluminescence quenching indicates a reduced number of oxygen defects upon Cs or BN introduction, suggesting the increase of photoinduced charge separation.

We previously reported that TiO_2-BN nanostructures display a band gap red shift and higher visible light absorption [80]. The band gap of the BN/1.5% Cs_2CO_3/TiO_2 sample was lower than that of Cs_2CO_3/TiO_2 samples due to the competing effects of a band gap blue-shift (size effect) and a band gap red-shift (BN exfoliation). This suggests that the additional modification of Cs_2CO_3-modified TiO_2 nanofibers with *h*-BN species may have a synergistic effect due to increased light absorption.

Table 1. Band gap values of pure TiO_2 nanofibers, and after modification with Cs_2CO_3 or/and BN

Sample	Band gap (eV)	Sample	Band gap (eV)
TiO_2	3.18±0.02	1.5% Cs_2CO_3/TiO_2	3.29±0.01
0.25% Cs_2CO_3/TiO_2	3.21±0.03	2.5% Cs_2CO_3/TiO_2	3.36±0.03
0.5% Cs_2CO_3/TiO_2	3.28±0.01	BN/TiO_2	3.16±0.02
1.0% Cs_2CO_3/TiO_2	3.27±0.02	BN/1.5% Cs_2CO_3/TiO_2	3.2±0.04

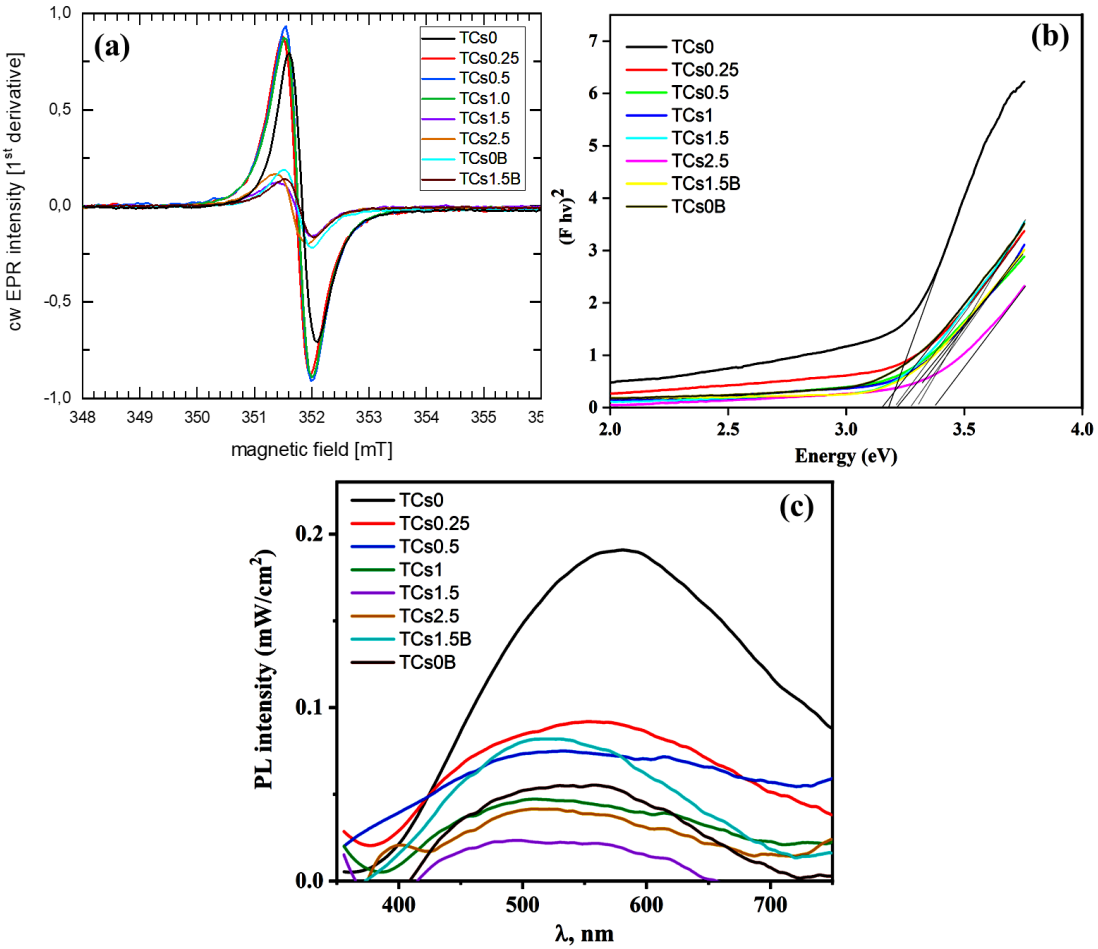

Fig. 4 (a) cw EPR measurements at room temperature of pristine TiO_2 (TCs0), 0.25% Cs_2CO_3/TiO_2 (TCs0.25), 0.5% Cs_2CO_3/TiO_2 (TCs0.5), 1% Cs_2CO_3/TiO_2 (TCs1), 1.5% Cs_2CO_3/TiO_2 (TCs1.5), 2.5% Cs_2CO_3/TiO_2 (TCs2.5), BN/TiO_2 (TCs0B), and BN/1.5% Cs_2CO_3/TiO_2 (TCs1.5B) (9.86 GHz mw frequency, modulation amplitude 2 G, modulation frequency 100 kHz). (b) Plot of the transformed Kubelka–Munk function versus light energy to calculate the band gap energy of TCs0, TCs0.25, TCs0.5, TCs1, TCs1.5, TCs2.5, TCs0B, and TCs1.5B. (c) Photoluminescence spectra of the TCs0, TCs0.25, TCs0.5, TCs1, TCs1.5, TCs2.5, TCs0B, and TCs1.5B samples.

3.2. Photoelectrochemical performance

Then, EIS was used to predict the mechanism of photocatalytic H_2 generation by the synthesized photocatalysts (Fig. 5a). The arc radius of Cs_2CO_3/TiO_2 electrodes was much smaller than that of the bare TiO_2 electrode. Moreover, the arc radius of BN/1.5% Cs_2CO_3/TiO_2 was smaller than those of bare TiO_2 and h-BN. This result further demonstrated that Cs_2CO_3/TiO_2 electrodes display a much higher separation efficiency of photogenerated e^-/h^+ pairs and a faster charge-transfer than the TiO_2 electrode at the solid–liquid interface. Therefore, Cs and BN incorporation in TiO_2 is an interesting strategy to enhance its

photocatalytic performance [81]. Impedance was significantly decreased after Cs_2CO_3 addition, indicating a lower charge transfer resistance across the electrode/electrolyte interface. The smallest arc radius was observed with the BN/1.5% Cs_2CO_3/TiO_2 electrode. Its lowest impedance can facilitate interfacial charge transfer and increase the separation efficiency of photoinduced carriers, thus enhancing photocatalysis efficiency.

3.2.2 H_2 generation reactions

The photocatalytic performance of the different nanofibers was investigated by monitoring H_2 generation by water splitting in an aqueous solution containing methanol as scavenger in the presence of visible light (Fig. 5b). Methanol molecules scavenge the holes, thus decreasing e^-/h^+ recombination, whereas electrons react with protons to produce H_2. Zhu *et al.*, Patra *et al.*, and Wang *et al.* described methanol role in photocatalytic reactions (Table 2). When using pristine TiO_2, H_2 production was low (110 $\mu mol \cdot g^{-1} \cdot h^{-1}$), due to the rapid e^-/h^+ recombination, fast backward reactions, and large energy band gap (3.19 eV) [82]. Cs_2CO_3 addition significantly increased H_2 production rate, suggesting that the heterojunction formed between Cs_2CO_3 and TiO_2 contributed to the efficient charge separation across the interface. Therefore, the enhanced photocatalytic activity can be explained by the synergistic effect of the heterojunction composition on increasing TiO_2 optical absorption and on decreasing e^-/h^+ recombination rate. Nada *et al.* evaluated the photocatalytic activity of Gd^{+3}-doped TiO_2 for H_2 production under visible light [34]. They found that metal ion doping influences TiO_2 photocatalytic activity by altering the band gap energy and conduction band position or the hole lifetime in the valence band. Moreover, doping led to lattice defects that acted as electron (or hole) traps, thus increasing the e^-/h^+ pair lifetime and the photocatalytic activity. Patra *et al.*, Lin *et al.*, and Lu *et al.* reported similar results on the photocatalytic activity of metal ion-doped TiO_2 (Table 2).

Comparison of the TiO_2 catalysts with different Cs_2CO_3 mol% (Fig. 5b) indicated that the best catalytic activity was obtained with the 1.5% Cs_2CO_3/TiO_2 sample (H_2 evolution rate of 9,853 $\mu mol \cdot g^{-1} \cdot h^{-1}$). With lower Cs_2CO_3 mol%, photocatalytic activity decreased, likely due to the absence of enough active sites to produce higher H_2 amounts. The 2.5% Cs_2CO_3/TiO_2 sample gave a H_2 evolution rate of 8,220 $\mu mol \cdot g^{-1} \cdot h^{-1}$. This decrease might be explained by Cs "shielding effect". Indeed, the photocatalytic activity decrease can be attributed to the following reasons: (i) increase in the opacity that leads to a decrease of the incident light absorption [83]; (ii) charge carrier recombination, (iii) catalyst agglomeration,

(iv) self-filtering effect, (v) higher light dispersion, and (vi) shadow effect of metals [9] [17] [52] [84-86].

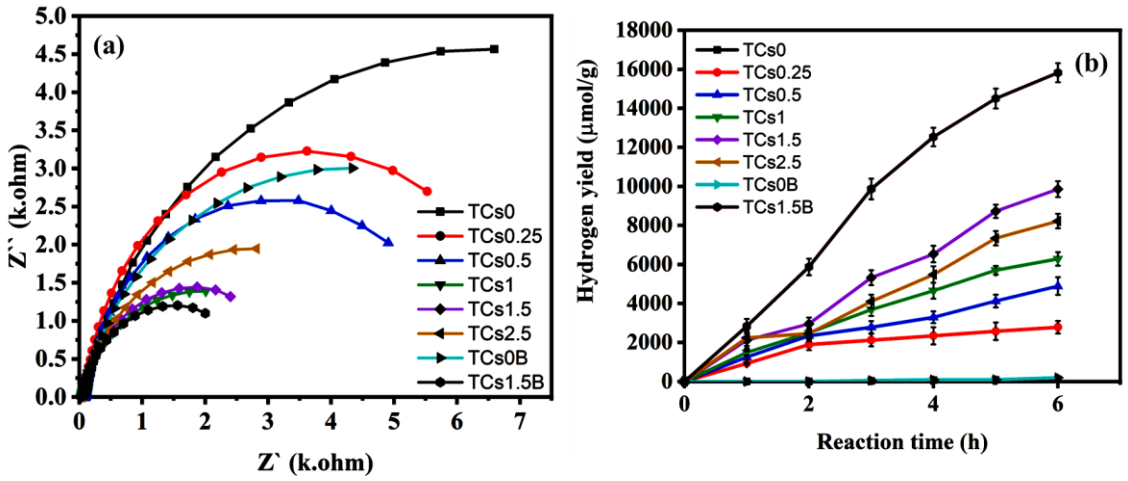

Fig. 8

Fig. 5 (a) EIS of pristine TiO_2 (TCs0), 0.25% Cs_2CO_3/TiO_2 (TCs0.25), 0.5% Cs_2CO_3/TiO_2 (TCs0.5), 1% Cs_2CO_3/TiO_2 (TCs1), 1.5% Cs_2CO_3/TiO_2 (TCs1.5), 2.5% Cs_2CO_3/TiO_2 (TCs2.5), BN/TiO_2 (TCs0B), and BN/1.5% Cs_2CO_3/TiO_2 (TCs1.5B) composites. (b) Photocatalytic performance (H_2 evolution rate) of the indicated catalysts.

Then, analysis of BN/TiO_2 and BN/1.5% Cs_2CO_3/TiO_2 photocatalytic activity (Fig. 5b) showed that the H_2 evolution rate increased from 110 $\mu mol \cdot g^{-1} \cdot h^{-1}$ with pristine TiO_2 to 194 $\mu mol \cdot g^{-1} \cdot h^{-1}$ with BN/TiO_2 and to 15,823 $\mu mol \cdot g^{-1} \cdot h^{-1}$ with BN/1.5% Cs_2CO_3/TiO_2 (i.e. the highest H_2 production capacity in this study). This outstanding performance could be due to the co-catalyst effect of BN on TiO_2 surface that limits e^-/h^+ recombination and enhances the photo-exciton lifetime [82]. Comparison of the present H_2 production yields with those of previous studies (Table 2) suggests that BN and Cs might play an important synergistic role in enhancing H_2 production by photocatalysis.

The photocatalytic mechanism of H_2 production in the presence of BN/1.5% Cs_2CO_3/TiO_2 composite nanofibers could be explained by the following observations: i) increase of the band gap after formation of the Cs_2CO_3 layer (as indicated by the optical properties of Cs_2CO_3/TiO_2 samples). The opposite effect was observed in SnO_2/Cs_2CO_3 composite nanofibers [87] where band gap reduction was explained by a shift of SnO_2 valence band [87]; ii) Cs_2CO_3 effect on the TiO_2 layer crystallization and/or the formation of new secondary phases by diffused Cs-related species [55]; iii) position shift of the TiO_2 conduction band and work function reduction upon Cs_2CO_3 deposition on TiO_2 [55]. However, no

significant changes in TiO_2 crystalline structure and optical properties were observed [55]. Therefore, Cs_2CO_3/TiO_2 interface defines charge separation, optical properties and photocatalytic properties. Moreover, it was reported that Cs_2CO_3 on metal oxide can be partially transformed into Cs oxides with low band gap [55, 88, 89]. However, peaks related to Cs oxides were not detected in the XRD spectra of our samples. On the basis of the Raman analysis results, it could be hypothesized that TiO_2/Cs_2CO_3 composites with amorphous phase and defect levels are formed at the TiO_2/Cs_2CO_3 interface. The defects support the transfer of photogenerated charges to TiO_2 band gap. The photogenerated holes and electrons are separated due to the formed interface layer. The suggested mechanism with the energy levels alignment is illustrated in Figure 6, where electron affinity (χ), work function (Φ) and band gap (E_g) are 2.2, 3.23 and 4.2 eV, respectively, for Cs_2CO_3 [88, 90] and 3.43, 4.23 and 3.2 eV, respectively, for TiO_2 [91]. In our work, the F1 and F2 (Fermi level of TiO_2 and Cs_2CO_3) were 0.80 eV and 1.03 eV, respectively. Thus the built-in potential (V_{bi}) was 0.23 eV and the ΔE_c and ΔE_v were -1.23 and 0.21 eV, respectively (Fig. 6). Moreover, BN role is important in reducing the e^-/h^+ recombination rate. BN is negatively charged and contacts the whole nanofiber surface. BN role is to capture photogenerated holes [92].

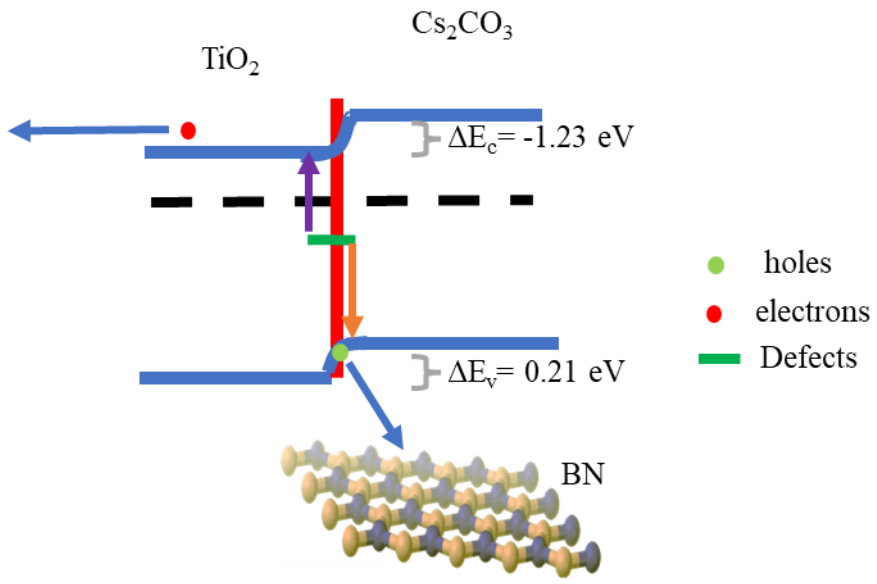

Fig. 6. Mechanism of H_2 production by photocatalysis in the presence of $BN/Cs_2CO_3/TiO_2$ and energy levels of $BN/Cs_2CO_3/TiO_2$ composite nanofibers. Arrows?

Table 2 summarizes the key findings about previously described metal- and non-metal-doped TiO_2 photocatalysts for H_2 production. The highest H_2 production was achieved

when metals were used as modifiers. Moreover, TiO_2 efficiency was significantly enhanced when more than one modifier was used, such as N, B-N and BN. These findings are in agreement with those reported in the present study. Compared with these photocatalysts, our composite nanofibers displayed a good photocatalytic activity.

Table 2. Metal and non-metal doped TiO_2 photocatalyst activity for H_2 evolution.

Catalyst	Preparation technique	H_2 (μmol g^{-1} h^{-1})	Sacrificial agent	Reference	Light source
BN/1.5% Cs_2CO_3/TiO_2	Electrospinning	2,638	Methanol	This work	500 W halogen lamp
1.5% Cs_2CO_3/TiO_2	Electrospinning	1,642	Methanol	This work	500W halogen lamp
Ga/N-TiO_2	Sol-gel	5.32	Methanol	[93]	125 W mercury lamp
BCN-TiO_2	High-temperature calcination	68.54	Tri-ethanolamine	[94]	300 W xenon lamp
Pt/B-N-TiO_2	Hydrothermal & heat treatment	8,200	Glycerol	[95]	300 W xenon lamp
Ag-Au/TiO_2	Photodeposition	718	Methanol	[96]	300 W, mercury lamp
Si,Fe-TiO_2	Sol-gel	2,000	Ethanol	[97]	500 W xenon lamp
g-C_3N_4/TiO_2	Sol-gel	560	Methanol	[98]	500 W xenon lamp

Lastly, the BN/1.5% Cs_2CO_3/TiO_2 photocatalyst stability and recyclability were monitored in four consecutive runs of 6 h under visible light irradiation (Fig. 7). H_2 production rate slightly decreased (not significantly) by 928 $\mu mol \cdot g^{-1} \cdot h^{-1}$ (i.e. ~6% of reduction), after four runs. This showed the excellent reusability and stability of BN/1.5% Cs_2CO_3/TiO_2 nanofibers.

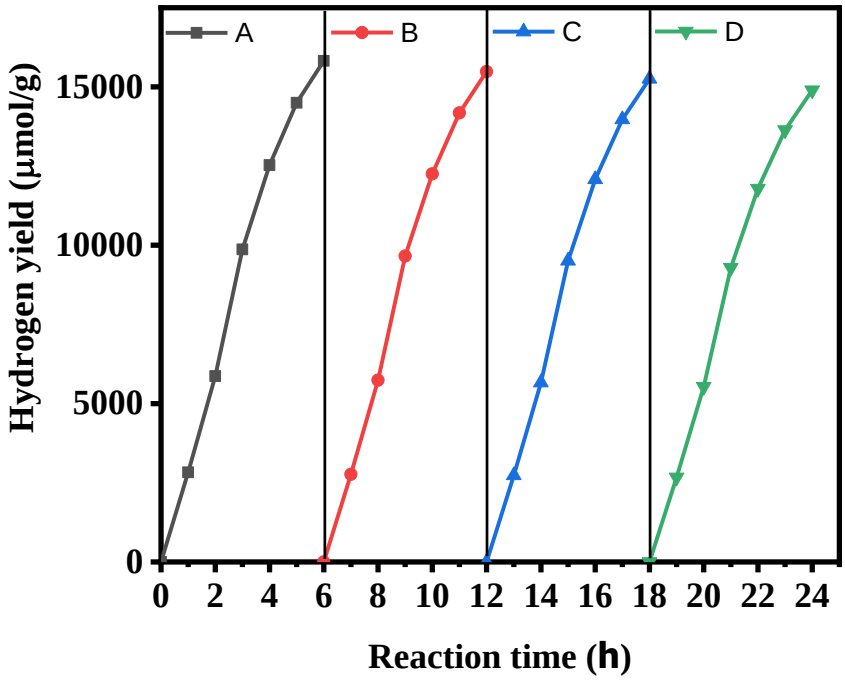

Fig. 7 Recycling test of BN/1.5% Cs_2CO_3/TiO_2.

4. Conclusion

This study reports the synergistic effect of Cs and BN on TiO_2 photocatalytic activity during water splitting under visible light irradiation. TiO_2 photocatalysts (with/without Cs and/or BN) were easily and efficiently generated using electrospinning. The characterization of their structural, morphological and optical properties highlighted the improved photocatalytic activity of Cs-modified TiO_2 nanofibers upon exposure to visible light compared with pristine TiO_2 nanofibers. Their photocatalytic activity was further improved by BN addition that reduced charge recombination. Specifically, the band gap was narrower and the photogenerated e^-/h^+ pair recombination was reduced in BN/TiO_2 compared with pristine and Cs-modified TiO_2 nanofibers. Holes were scavenged rapidly by *h*-BN nanosheets due to the electrostatic attraction between the hole positive charge and BN negative charge. In addition, BN on TiO_2 surface contributed to promote e^-/h^+ separation and to extend the photo-excitons lifetime. The BN/1.5% Cs_2CO_3/TiO_2 nanocomposite showed the best photocatalytic activity for H_2 production, *i.e.* 143 times higher than that of pristine TiO_2.

Acknowledgements

This work was supported by the French Government through a scholarship granted by the French Embassy in IRAN. The authors thank *University of Zanjan* and *Université de Montpellier* for financial support to this study.

REFERENCES

[1] H. Hou, Y. Pan, G. Bai, Y. Li, V. Murugadoss, Y. Zhao, High-throughput computing for hydrogen transport properties in ε-ZrH2, Advanced Composites and Hybrid Materials, 5 (2022) 1350-1361.
[2] S.L. Hamukwaya, Z. Zhao, H. Hao, H.M. Abo-Dief, K.M. Abualnaja, A.K. Alanazi, M.M. Mashingaidze, S.M. El-Bahy, M. Huang, Z. Guo, Enhanced photocatalytic performance for hydrogen production and carbon dioxide reduction by a mesoporous single-crystal-like TiO2 composite catalyst, Advanced Composites and Hybrid Materials, 5 (2022) 2620-2630.
[3] G. Roymahapatra, M.K. Dash, A. Ghosh, A. Bag, S. Mishra, S. Maity, Hydrogen storage on Lithium chloride/Lithium bromide surface at cryogenic temperature, ES Energy & Environment, 18 (2022) 90-100.
[4] X. Pan, Z. Zheng, X. Zhang, X. He, Y. An, Y. Hao, K. Huang, M. Lei, Multi-metallic Nanosheets for High-performance Hydrogen Evolution Reaction, Engineered Science, 19 (2022) 253-261.
[5] G. Roymahapatra, M.K. Dash, S. Sinha, G. Ch, Z. Guo, Theoretical Investigation of Hydrogen Adsorption Efficiency of [Oxadiazole-xLi+] Complexes (x= 1, 2): In Pursuit of Green Fuel Storage, Engineered Science, 19 (2022) 114-124.
[6] M.K. Dash, S.D. Chowdhury, R. Chatterjee, S. Maity, G. Roymahapatra, M. Huang, M. Nath, Z. Guo, Computational Investigation on Lithium Fluoride for Efficient Hydrogen Storage System, Engineered Science, 18 (2022) 98-104.
[7] A. Kudo, Y. Miseki, Heterogeneous photocatalyst materials for water splitting, Chemical Society Reviews, 38 (2009) 253-278.
[8] J. Sun, Q. Mu, H. Kimura, V. Murugadoss, M. He, W. Du, C. Hou, Oxidative degradation of phenols and substituted phenols in the water and atmosphere: a review, Advanced Composites and Hybrid Materials, 5 (2022) 627-640.
[9] X. Chen, S. Shen, L. Guo, S.S. Mao, Semiconductor-based photocatalytic hydrogen generation, Chemical reviews, 110 (2010) 6503-6570.
[10] Y. Zheng, Y. Jiao, M. Jaroniec, S.Z. Qiao, Advancing the electrochemistry of the hydrogen-evolution reaction through combining experiment and theory, Angewandte Chemie International Edition, 54 (2015) 52-65.
[11] F. Yao, W. Xie, C. Ma, D. Wang, Z.M. El-Bahy, M.H. Helal, H. Liu, A. Du, Z. Guo, H. Gu, Superb electromagnetic shielding polymer nanocomposites filled with 3-dimensional p-phenylenediamine/aniline copolymer nanofibers@ copper foam hybrid nanofillers, Composites Part B: Engineering, 245 (2022) 110236.
[12] X. Zou, Y. Zhang, Noble metal-free hydrogen evolution catalysts for water splitting, Chemical Society Reviews, 44 (2015) 5148-5180.
[13] I. Roger, M.A. Shipman, M.D. Symes, Earth-abundant catalysts for electrochemical and photoelectrochemical water splitting, Nature Reviews Chemistry, 1 (2017) 1-13.
[14] K. Sivula, R. Van De Krol, Semiconducting materials for photoelectrochemical energy conversion, Nature Reviews Materials, 1 (2016) 1-16.
[15] J. Tian, Z. Zhao, A. Kumar, R.I. Boughton, H. Liu, Recent progress in design, synthesis, and applications of one-dimensional TiO 2 nanostructured surface heterostructures: a review, Chemical Society Reviews, 43 (2014) 6920-6937.

[16] P.-K. Chuang, K.-H. Wu, T.-F. Yeh, H. Teng, Extending the π-conjugation of g-C3N4 by incorporating aromatic carbon for photocatalytic H2 evolution from aqueous solution, ACS Sustainable Chemistry & Engineering, 4 (2016) 5989-5997.
[17] C. Dang, Q. Mu, X. Xie, X. Sun, X. Yang, Y. Zhang, S. Maganti, M. Huang, Q. Jiang, I. Seok, Recent progress in cathode catalyst for nonaqueous lithium oxygen batteries: a review, Advanced Composites and Hybrid Materials, 5 (2022) 606-626.
[18] L. Ge, C. Han, X. Xiao, L. Guo, Synthesis and characterization of composite visible light active photocatalysts MoS2–g-C3N4 with enhanced hydrogen evolution activity, International journal of hydrogen energy, 38 (2013) 6960-6969.
[19] A. Fujishima, K. Honda, Electrochemical photolysis of water at a semiconductor electrode, nature, 238 (1972) 37-38.
[20] V. Kumaravel, S. Mathew, J. Bartlett, S.C. Pillai, Photocatalytic hydrogen production using metal doped TiO2: A review of recent advances, Applied Catalysis B: Environmental, 244 (2019) 1021-1064.
[21] Y. Ma, X. Xie, W. Yang, Z. Yu, X. Sun, Y. Zhang, X. Yang, H. Kimura, C. Hou, Z. Guo, Recent advances in transition metal oxides with different dimensions as electrodes for high-performance supercapacitors, Advanced Composites and Hybrid Materials, 4 (2021) 906-924.
[22] C. Hou, B. Wang, V. Murugadoss, S. Vupputuri, Y. Chao, Z. Guo, C. Wang, W. Du, Recent advances in Co3O4 as anode materials for high-performance lithium-ion batteries, Engineered Science, 11 (2020) 19-30.
[23] A. Arun, P. Malrautu, A. Laha, S. Ramakrishna, Gelatin nanofibers in drug delivery systems and tissue engineering, Engineered Science, 16 (2021) 71-81.
[24] X. Hong, J. Tan, H. Zhu, N. Feng, Y. Yang, J.T. Irvine, L. Wang, G. Liu, H.M. Cheng, Control of Spatially Homogeneous Distribution of Heteroatoms to Produce Red TiO2 Photocatalyst for Visible-Light Photocatalytic Water Splitting, Chemistry–A European Journal, 25 (2019) 1787-1794.
[25] C. Jing, Y. Zhang, J. Zheng, S. Ge, J. Lin, D. Pan, N. Naik, Z. Guo, In-situ constructing visible light CdS/Cd-MOF photocatalyst with enhanced photodegradation of methylene blue, Particuology, 69 (2022) 111-122.
[26] S. Ikeda, N. Sugiyama, B. Pal, G. Marcí, L. Palmisano, H. Noguchi, K. Uosaki, B. Ohtani, Photocatalytic activity of transition-metal-loaded titanium (IV) oxide powders suspended in aqueous solutions: Correlation with electron–hole recombination kinetics, Physical chemistry chemical physics, 3 (2001) 267-273.
[27] C. Minero, G. Mariella, V. Maurino, E. Pelizzetti, Photocatalytic transformation of organic compounds in the presence of inorganic anions. 1. Hydroxyl-mediated and direct electron-transfer reactions of phenol on a titanium dioxide− fluoride system, Langmuir, 16 (2000) 2632-2641.
[28] F. Xu, J. Zhang, B. Zhu, J. Yu, J. Xu, CuInS2 sensitized TiO2 hybrid nanofibers for improved photocatalytic CO2 reduction, Applied Catalysis B: Environmental, 230 (2018) 194-202.
[29] Z. Li, W. Xie, F. Yao, A. Du, Q. Wang, Z. Guo, H. Gu, Comprehensive electrocatalytic degradation of tetracycline in wastewater by electrospun perovskite manganite nanoparticles supported on carbon nanofibers, Advanced Composites and Hybrid Materials, 5 (2022) 2092-2105.
[30] W. Zhang, Y. Feng, J.T. Althakafy, Y. Liu, H.M. Abo-Dief, M. Huang, L. Zhou, F. Su, C. Liu, C. Shen, Ultrahigh molecular weight polyethylene fiber/boron nitride composites with high neutron shielding efficiency and mechanical performance, Advanced Composites and Hybrid Materials, 5 (2022) 2012-2020.
[31] J. Chen, F. Qiu, W. Xu, S. Cao, H. Zhu, Recent progress in enhancing photocatalytic efficiency of TiO2-based materials, Applied Catalysis A: General, 495 (2015) 131-140.
[32] J. Xu, P. Zhu, I.H. El Azab, B.B. Xu, Z. Guo, A.Y. Elnaggar, G.A. Mersal, X. Liu, Y. Zhi, Z. Lin, An efficient bifunctional Ni-Nb2O5 nanocatalysts for the hydrodeoxygenation of anisole, Chinese Journal of Chemical Engineering, 49 (2022) 187-197.
[33] J. Biscarat, M. Bechelany, C. Pochat-Bohatier, P. Miele, Graphene-like BN/gelatin nanobiocomposites for gas barrier applications, Nanoscale, 7 (2015) 613-618.

[34] A.A. Nada, M.F. Bekheet, R. Viter, P. Miele, S. Roualdes, M. Bechelany, BN/GdxTi (1-x) O (4-x)/2 nanofibers for enhanced photocatalytic hydrogen production under visible light, Applied Catalysis B: Environmental, 251 (2019) 76-86.
[35] L. Yang, W.W.F. Leung, Electrospun TiO2 nanorods with carbon nanotubes for efficient electron collection in dye-sensitized solar cells, Advanced Materials, 25 (2013) 1792-1795.
[36] X. Xu, F. Yao, O.A.A. Ali, W. Xie, S.F. Mahmoud, P. Xie, S.M. El-Bahy, M. Huang, C. Liu, R. Fan, Adjustable core-sheath architecture of polyaniline-decorated hollow carbon nanofiber nanocomposites with negative permittivity for superb electromagnetic interference shielding, Advanced Composites and Hybrid Materials, 5 (2022) 2002-2011.
[37] H. Tada, A. Hattori, Y. Tokihisa, K. Imai, N. Tohge, S. Ito, A patterned-TiO2/SnO2 bilayer type photocatalyst, the Journal of Physical Chemistry B, 104 (2000) 4585-4587.
[38] F. Zhang, M. Lian, A. Alhadhrami, M. Huang, B. Li, G.A. Mersal, M.M. Ibrahim, M. Xu, Laccase immobilized on functionalized cellulose nanofiber/alginate composite hydrogel for efficient bisphenol A degradation from polluted water, Advanced Composites and Hybrid Materials, 5 (2022) 1852-1864.
[39] D. Li, Y. Xia, Electrospinning of nanofibers: reinventing the wheel?, Advanced materials, 16 (2004) 1151-1170.
[40] L. Li, B. Cheng, Y. Wang, J. Yu, Enhanced photocatalytic H2-production activity of bicomponent NiO/TiO2 composite nanofibers, Journal of colloid and interface science, 449 (2015) 115-121.
[41] Z. Sun, M. Wang, J. Fan, R. Feng, Y. Zhou, L. Zhang, TiO2@ MIL-101 (Cr) nanocomposites as an efficient photocatalyst for degradation of toluene, Advanced Composites and Hybrid Materials, 4 (2021) 1322-1329.
[42] S. Chuangchote, J. Jitputti, T. Sagawa, S. Yoshikawa, Photocatalytic activity for hydrogen evolution of electrospun TiO2 nanofibers, ACS applied materials & interfaces, 1 (2009) 1140-1143.
[43] F. Zhang, W. Cheng, Z. Yu, S. Ge, Q. Shao, D. Pan, B. Liu, X. Wang, Z. Guo, Microwave hydrothermally synthesized WO3/UiO-66 nanocomposites toward enhanced photocatalytic degradation of rhodamine B, Advanced Composites and Hybrid Materials, 4 (2021) 1330-1342.
[44] X. Chen, S.S. Mao, Synthesis of titanium dioxide (TiO2) nanomaterials, Journal of nanoscience and nanotechnology, 6 (2006) 906-925.
[45] E. Stathatos, P. Lianos, F. Del Monte, D. Levy, D. Tsiourvas, Formation of TiO2 nanoparticles in reverse micelles and their deposition as thin films on glass substrates, Langmuir, 13 (1997) 4295-4300.
[46] Y. Yue, Z. Gao, Synthesis of mesoporous TiO2 with a crystalline framework, Chemical Communications, (2000) 1755-1756.
[47] L.G. Devi, S.G. Kumar, B.N. Murthy, N. Kottam, Influence of Mn2+ and Mo6+ dopants on the phase transformations of TiO2 lattice and its photo catalytic activity under solar illumination, Catalysis Communications, 10 (2009) 794-798.
[48] A. Hezam, K. Namratha, Q. Drmosh, D. Ponnamma, A.M.N. Saeed, V. Ganesh, B. Neppolian, K. Byrappa, Direct Z-scheme Cs 2 O–Bi 2 O 3–ZnO heterostructures for photocatalytic overall water splitting, Journal of Materials Chemistry A, 6 (2018) 21379-21388.
[49] A. Kudo, T. Kondo, Photoluminescent and photocatalytic properties of layered caesiumtitanates, Cs2TinO2n+ 1 (n= 2, 5, 6), Journal of Materials Chemistry, 7 (1997) 777-780.
[50] M. Nasr, R. Viter, C. Eid, R. Habchi, P. Miele, M. Bechelany, Enhanced photocatalytic performance of novel electrospun BN/TiO 2 composite nanofibers, New Journal of Chemistry, 41 (2017) 81-89.
[51] A.A. Nada, M. Nasr, R. Viter, P. Miele, S.p. Roualdes, M. Bechelany, Mesoporous ZnFe2O4@ TiO2 nanofibers prepared by electrospinning coupled to PECVD as highly performing photocatalytic materials, The Journal of Physical Chemistry C, 121 (2017) 24669-24677.

[52] K.K. Mandari, A.K.R. Police, J.Y. Do, M. Kang, C. Byon, Rare earth metal Gd influenced defect sites in N doped TiO2: defect mediated improved charge transfer for enhanced photocatalytic hydrogen production, International Journal of Hydrogen Energy, 43 (2018) 2073-2082.
[53] A.A. Nada, W.M. El Rouby, M.F. Bekheet, M. Antuch, M. Weber, P. Miele, R. Viter, S. Roualdes, P. Millet, M. Bechelany, Highly textured boron/nitrogen co-doped TiO2 with honeycomb structure showing enhanced visible-light photoelectrocatalytic activity, Applied Surface Science, 505 (2020) 144419.
[54] Y. Yuan, D. Li, J. Xu, H. Wang, X. Xue, F. Hu, X. Zhang, All solution-processed composite (ZnO+ PEG)/Cs2CO3 with robust electron injection tailoring and its application to efficient inverted near ultraviolet organic light-emitting diodes, Synthetic Metals, 278 (2021) 116828.
[55] W.H. Kim, S. Woo, K.-P. Kim, S.-M. Kwon, D.-H. Kim, Efficient TiO2 surface treatment using Cs2CO3 for solution-processed planar-type Sb2S3 solar cells, Nanoscale Research Letters, 14 (2019) 1-9.
[56] S.J. Doh, C. Kim, S.G. Lee, S.J. Lee, H. Kim, Development of photocatalytic TiO2 nanofibers by electrospinning and its application to degradation of dye pollutants, Journal of hazardous materials, 154 (2008) 118-127.
[57] R.D. Shannon, Revised effective ionic radii and systematic studies of interatomic distances in halides and chalcogenides, Acta crystallographica section A: crystal physics, diffraction, theoretical and general crystallography, 32 (1976) 751-767.
[58] M. Ghorbanloo, A.A. Nada, H.H. El-Maghrabi, M.F. Bekheet, W. Riedel, B. Djamel, R. Viter, S. Roualdes, F.S. Soliman, Y.M. Moustafa, Superior efficiency of BN/Ce2O3/TiO2 nanofibers for photocatalytic hydrogen generation reactions, Applied Surface Science, 594 (2022) 153438.
[59] Y. Qiu, J. Yu, J. Yin, C. Tan, X. Zhou, X. Bai, E. Wang, Synthesis of continuous boron nitride nanofibers by solution coating electrospun template fibers, Nanotechnology, 20 (2009) 345603.
[60] J. Wang, P. Wang, Y. Cao, J. Chen, W. Li, Y. Shao, Y. Zheng, D. Li, A high efficient photocatalyst Ag3VO4/TiO2/graphene nanocomposite with wide spectral response, Applied Catalysis B: Environmental, 136 (2013) 94-102.
[61] S.D. Perera, R.G. Mariano, K. Vu, N. Nour, O. Seitz, Y. Chabal, K.J. Balkus Jr, Hydrothermal synthesis of graphene-TiO2 nanotube composites with enhanced photocatalytic activity, Acs Catalysis, 2 (2012) 949-956.
[62] Y. Sheng, J. Yang, F. Wang, L. Liu, H. Liu, C. Yan, Z. Guo, Sol-gel synthesized hexagonal boron nitride/titania nanocomposites with enhanced photocatalytic activity, Applied Surface Science, 465 (2019) 154-163.
[63] Y. Shi, C. Hamsen, X. Jia, K.K. Kim, A. Reina, M. Hofmann, A.L. Hsu, K. Zhang, H. Li, Z.-Y. Juang, Synthesis of few-layer hexagonal boron nitride thin film by chemical vapor deposition, Nano letters, 10 (2010) 4134-4139.
[64] H.J. Jung, K. Nam, H.-G. Sung, H.S. Hyun, Y. Sohn, W.G. Shin, Preparation of TiO2-decorated boron particles by wet ball milling and their photoelectrochemical hydrogen and oxygen evolution reactions, Materials, 9 (2016) 1012.
[65] V. Yadav, V. Kulshrestha, Boron nitride: a promising material for proton exchange membranes for energy applications, Nanoscale, 11 (2019) 12755-12773.
[66] S. Ahmad, A. Sultan, W. Raza, M. Muneer, F. Mohammad, Boron nitride based polyaniline nanocomposite: Preparation, property, and application, Journal of Applied Polymer Science, 133 (2016).
[67] D. Weathers, S. Sharma, S.L. Wood, Effects of online communication practices on consumer perceptions of performance uncertainty for search and experience goods, Journal of retailing, 83 (2007) 393-401.
[68] C. Hou, W. Yang, H. Kimura, X. Xie, X. Zhang, X. Sun, Z. Yu, X. Yang, Y. Zhang, B. Wang, Boosted lithium storage performance by local build-in electric field derived by oxygen vacancies in 3D holey

N-doped carbon structure decorated with molybdenum dioxide, Journal of Materials Science & Technology, 142 (2023) 185-195.
[69] W. Yang, D. Peng, H. Kimura, X. Zhang, X. Sun, R.A. Pashameah, E. Alzahrani, B. Wang, Z. Guo, W. Du, Honeycomb-like nitrogen-doped porous carbon decorated with Co3O4 nanoparticles for superior electrochemical performance pseudo-capacitive lithium storage and supercapacitors, Advanced Composites and Hybrid Materials, 5 (2022) 3146-3157.
[70] Y. Zhang, L. Liu, L. Zhao, C. Hou, M. Huang, H. Algadi, D. Li, Q. Xia, J. Wang, Z. Zhou, Sandwich-like CoMoP2/MoP heterostructures coupling N, P co-doped carbon nanosheets as advanced anodes for high-performance lithium-ion batteries, Advanced Composites and Hybrid Materials, 5 (2022) 2601-2610.
[71] C. Naccache, P. Meriaudeau, M. Che, A. Tench, Identification of oxygen species adsorbed on reduced titanium dioxide, Transactions of the Faraday Society, 67 (1971) 506-512.
[72] A. Volodin, A. Cherkashin, V. Zakharenko, Influence of physically adsorbed oxygen on the separation of electron-hole pairs on anatase irradiated by visible light, Reaction Kinetics and Catalysis Letters, 11 (1979) 103-106.
[73] E. Serwicka, M. Schlierkamp, R. Schindler, Localization of Conduction Band Electrons in Polycrystalline Ti02 Studied by ESR, Zeitschrift für Naturforschung A, 36 (1981) 226-232.
[74] I. Nakamura, N. Negishi, S. Kutsuna, T. Ihara, S. Sugihara, K. Takeuchi, Role of oxygen vacancy in the plasma-treated TiO2 photocatalyst with visible light activity for NO removal, Journal of Molecular Catalysis A: Chemical, 161 (2000) 205-212.
[75] H. Zong, Y.-H. Lou, M. Li, K.-L. Wang, S.M. Jain, Z.-K. Wang, Improved open-circuit voltage via Cs2CO3-Doped TiO2 for high-performance and stable perovskite solar cells, Organic Electronics, 77 (2020) 105495.
[76] L. Qin, Z. Xie, L. Yao, Y. Yan, S. Pang, F. Wei, G. Qin, Enhancing the efficiency of TiO2–perovskite heterojunction solar cell via evaporating Cs2CO3 on TiO2, physica status solidi (RRL)–Rapid Research Letters, 8 (2014) 912-916.
[77] M.H. Park, J.H. Li, A. Kumar, G. Li, Y. Yang, Doping of the metal oxide nanostructure and its influence in organic electronics, Advanced Functional Materials, 19 (2009) 1241-1246.
[78] J. Liu, L. Zhu, S. Xiang, H. Wang, H. Liu, W. Li, H. Chen, Cs-doped TiO2 nanorod array enhances electron injection and transport in carbon-based CsPbI3 perovskite solar cells, ACS Sustainable Chemistry & Engineering, 7 (2019) 16927-16932.
[79] M. Nasr, A. Abou Chaaya, N. Abboud, M. Bechelany, R. Viter, C. Eid, A. Khoury, P. Miele, Photoluminescence: A very sensitive tool to detect the presence of anatase in rutile phase electrospun TiO2 nanofibers, Superlattices and Microstructures, 77 (2015) 18-24.
[80] S. Sayegh, F. Tanos, A. Nada, G. Lesage, F. Zaviska, E. Petit, V. Rouessac, I. Iatsunskyi, E. Coy, R. Viter, Tunable TiO 2–BN–Pd nanofibers by combining electrospinning and atomic layer deposition to enhance photodegradation of acetaminophen, Dalton Transactions, 51 (2022) 2674-2695.
[81] Z. Liu, Q. Wang, X. Tan, S. Zheng, H. Zhang, Y. Wang, S. Gao, Solvothermal preparation of Bi/Bi2O3 nanoparticles on TiO2 NTs for the enhanced photoelectrocatalytic degradation of pollutants, Journal of Alloys and Compounds, 815 (2020) 152478.
[82] N. Li, H. Huang, R. Bibi, Q. Shen, R. Ngulube, J. Zhou, M. Liu, Noble-metal-free MOF derived hollow CdS/TiO2 decorated with NiS cocatalyst for efficient photocatalytic hydrogen evolution, Applied Surface Science, 476 (2019) 378-386.
[83] Z. Sun, Y. Zhang, S. Guo, J. Shi, C. Shi, K. Qu, H. Qi, Z. Huang, V. Murugadoss, M. Huang, Confining FeNi nanoparticles in biomass-derived carbon for effectively photo-Fenton catalytic reaction for polluted water treatment, Advanced Composites and Hybrid Materials, 5 (2022) 1566-1581.
[84] N.J. Vickers, Animal communication: when i'm calling you, will you answer too?, Current biology, 27 (2017) R713-R715.

[85] F. López-Tenllado, J. Hidalgo-Carrillo, V. Montes, A. Marinas, F. Urbano, J. Marinas, L. Ilieva, T. Tabakova, F. Reid, A comparative study of hydrogen photocatalytic production from glycerol and propan-2-ol on M/TiO2 systems (M= Au, Pt, Pd), Catalysis Today, 280 (2017) 58-64.
[86] J. Jiang, X. Zhang, P. Sun, L. Zhang, ZnO/BiOI heterostructures: photoinduced charge-transfer property and enhanced visible-light photocatalytic activity, The Journal of Physical Chemistry C, 115 (2011) 20555-20564.
[87] V.-H. Tran, S.H. Eom, S.C. Yoon, S.-K. Kim, S.-H. Lee, Enhancing device performance of inverted organic solar cells with SnO2/Cs2CO3 as dual electron transport layers, Organic Electronics, 68 (2019) 85-95.
[88] H.-H. Liao, L.-M. Chen, Z. Xu, G. Li, Y. Yang, Highly efficient inverted polymer solar cell by low temperature annealing of Cs 2 CO 3 interlayer, Applied physics letters, 92 (2008) 156.
[89] J. Huang, Z. Xu, Y. Yang, Low-work-function surface formed by solution-processed and thermally deposited nanoscale layers of cesium carbonate, Advanced Functional Materials, 17 (2007) 1966-1973.
[90] C.-M. Chen, Z.-K. Lin, W.-J. Huang, S.-H. Yang, WO3 nanoparticles or nanorods incorporating Cs2CO3/PCBM buffer bilayer as carriers transporting materials for perovskite solar cells, Nanoscale research letters, 11 (2016) 1-11.
[91] S. Singh Surah, M. Vishwakarma, R. Kumar, R. Nain, S. Sirohi, G. Kumar, Tuning the electronic band alignment properties of TiO2 nanotubes by boron doping, Results in Physics, 12 (2019) 1725-1731.
[92] V. Štengl, J. Henych, M. Slušná, h-BN-TiO2 nanocomposite for photocatalytic applications, Journal of Nanomaterials, 2016 (2016).
[93] X. Li, Q. Liu, X. Jiang, J. Huang, Enhanced photocatalytic activity of Ga-N Co-doped anatase TiO2 for water decomposition to hydrogen, Int. J. Electrochem. Sci, 7 (2012) 11519-11527.
[94] X. Xing, H. Zhu, M. Zhang, L. Xiao, Q. Li, J. Yang, Effect of heterojunctions and phase-junctions on visible-light photocatalytic hydrogen evolution in BCN-TiO2 photocatalysts, Chemical Physics Letters, 727 (2019) 11-18.
[95] N. Luo, Z. Jiang, H. Shi, F. Cao, T. Xiao, P.P. Edwards, Photo-catalytic conversion of oxygenated hydrocarbons to hydrogen over heteroatom-doped TiO2 catalysts, international journal of hydrogen energy, 34 (2009) 125-129.
[96] K.K. Patra, C.S. Gopinath, Bimetallic and Plasmonic Ag–Au on TiO2 for Solar Water Splitting: An Active Nanocomposite for Entire Visible-Light-Region Absorption, ChemCatChem, 8 (2016) 3294-3311.
[97] Y. Lin, Z. Jiang, C. Zhu, X. Hu, H. Zhu, X. Zhang, J. Fan, S.H. Lin, The optical absorption and hydrogen production by water splitting of (Si, Fe)-codoped anatase TiO2 photocatalyst, International journal of hydrogen energy, 38 (2013) 5209-5214.
[98] J. Wang, J. Huang, H. Xie, A. Qu, Synthesis of g-C3N4/TiO2 with enhanced photocatalytic activity for H2 evolution by a simple method, International Journal of Hydrogen Energy, 39 (2014) 6354-6363.